Grasping via entanglement. Supplementary information.

Kaitlyn P. Becker[1], *Clark B. Teeple*[1], *Nicholas Charles*[1], *L. Mahadevan*[1,2,*], *Robert J. Wood*[1,*]

[1]School of Engineering and Applied Sciences, Harvard University, Cambridge, MA, USA

[2]Departments of Physics, and Organismic and Evolutionary Biology, Harvard University, Cambridge, MA, USA

*To whom correspondence should be addressed;

E-mail: lmahadev@g.harvard.edu, rjwood@seas.harvard.edu

Gripper Hardware

The gripper used for all of the physical tests in this work is comprised of twelve silicone filaments attached to a 3D printed palm, (manifold). The filaments were approximately $260\,\mathrm{mm}$ in length and $4.5\,\mathrm{mm}$ in diameter prior to actuation. The filaments were mounted to polypropylene and nylon luer lock plug to barb fittings (Mcmaster PN51525K141, PN51525K121) on one end and sealed at the other end. The luer lock fittings mounted in the end of the filaments attached to a 3D-printed manifold via nickel coated brass threaded luer lock sockets (Mcmaster PN51465K161). This allowed for modular repairs and replacing individual filaments in the case of a leak. This is in contrast to recent work where the filaments were fabricated as part of an integrated soft structure.[1] The individual ports on the manifold could also be closed with luer lock end plugs (Mcmaster PN51525K311) for fewer numbers of filaments and easily rearranged for different array formations, although the testing in this study utilized all twelve ports for all of the experiments. The Manifold was printed in a semi transparent resin (Stratysys veroclear OBJ-03271) on a Stratasys polyjet 3D printer. Three different mounting attachments were used for (1) mounting to the robot arm for grasp testing, (2) mounting in the materials characterization system (Instron 5544A) the for grip strength tests, and (3) mounting on a ROV for deep-sea tests. For all of the tests, however, the configuration of the ports on the distal portion of the gripper remained the same. The ports were evenly spaced in two concentric circles. The outer circle had diameter $50\,\mathrm{mm}$ and contained eight of the twelve ports arranged, while the inner circle had a diameter of $25\,\mathrm{mm}$ and contained the remaining four of twelve filaments.

Filament Fabrication

The actuators in this work were made from silicone rubber, Elastosil m4601 (Wacker Chemie) because of its high elongation to failure (700%), high tearing force, and relatively low cost. The rubber filaments were formed by dip molded silicone onto 305 mm (12 in) long stainless steel pins (McMaster-Carr 88915K11) following the fabrication methods presented by Becker et al.[1] The pins (or rods) are coated with liquid silicone rubber and then fixed at a 10 degree angle from vertical until the rubber is cured to create a thicker coating on one side of the rod. For the fabrication of the filaments, it was easier to suspend the rods from above. For successive coatings, the rods remained suspended between coatings. The filaments used for the tests in this study were formed with four coatings on pins that were $10\,\text{deg}$ from vertical. Once the silicone is cured and the rod is removed, the silicone forms a tube that has a thicker wall on one side where the coating pooled due to gravity. The rubber does not stick to the stainless steel and can be removed without the use of mold release, which is important because mold release could migrate during dipping and would thus create a risk of thin spots and holes in the sidewalls of the actuators.

To ease the release of actuators off of longer pins, the pin was pulled off of the dipping fixture and the ends of silicone trimmed while still on the pin. Removal of the silicone from the pin was aided by 15-30psi of air pressure was applied via a 1/16in hose barb into one side of the silicone. This does not create a perfect seal but supplies enough internal pressure to cause the actuators to expanded and slip off of the pin more easily. This demolding pressure may be modulated depending on the operating pressure of the actuators. Care was taken to apply tension to the actuator during removal from the pin so that, if the barb slipped and the internal pressure dropped, the actuator did not snap back and stretch over the tip of the pin, potentially creating a weak spot or pin hole.

For shorter pins, the full length may be dipped in a cup of rubbed and allowed to cure. For long pins, to avoid the need for large dipping vessels and wasted rubber, a cup with a hole in the bottom was used for the dip coating process. To help with this modified dip coating process for long pins, the pins were suspended from above. The cup was held at the top of the pin, filled with uncured rubber, slowly pulled down the length of the pin, and removed off of the lower free end of the pin.

Various fabrication variables can be altered to tune the functionality of the actuators, but the recipe used for the filaments tested in this paper was four dips coating of the Elastosil rubber, mixed with a 9:1 weight ration, as directed by the product information. The rubber was mixed for two rounds of 30s at 2000 rpm in a Thinky mixer and immediately applied to the pins and then allowed to cure a room temperature before adding another layer. The pins were fix at an angle of ten degrees from vertical until fully cured.

After removing the actuators from their forming pins, one end was sealed using Sil-Poxy (Smooth-On Ic.) or newly mixed Elastosil. For filaments used in a deep-sea field test, 1/16” diameter, 1/4” long steel pins were inserted into the end before sealing it. This served the purpose of weighting the ends to make them settle down faster after being moved through the water. The filaments otherwise drift in the water and are harder to direct. The pins also allowed the ends of the filaments to stick to a magnet on the ROV holster to keep them from drifting around until deployment. The remaining end of the filament was fixed onto a plastic 1/16” Luer-lok barb (part listed above) and secured with some Sil-Poxy and a wrapping of cotton twine (McMaster-Carr PN1929T12). After all Sil-Poxy and rubber is fully set, the Luer-lok fitting could then be attached to the gripper manifold as described above.

Object Set for Grasp Testing

The object set used for the experimental testing in this study is shown in Figure S1 and the object masses, materials, and characteristic dimensions are listed in Table S1. The tubes and sphere were selected to represent a few variants on simple geometric primitives similar to the YCB object set.[2] The torus and branched structures were included to introduce a set of objects for testing that are more topologically complex. The simple branched structures are more complex than the objects in the YCB object set but simple enough be reproduced on widely available FDM printers and simple enough to be implemented in simulations without high computational cost. In addition to the branched structures discussed in the main text, further variants are included in Figure S1 and Table S1. These variants and additional testing with them are discussed below.

Within the set of simple branched structures, (trees), used for testing, we explored the effect of two geometric parameters, (branch angle and branch number), on the grasping success with the entanglement grasping strategy. The number of branches (distributed evenly between two rings on the trunk) and the angle between branches and the trunk were varied as shown in S1 and Table S1. The other characteristic dimensions were held constant, including the the trunk height of $120\,\mathrm{mm}$, trunk diameter of $10\,\mathrm{mm}$, branch diameter of $7\,\mathrm{mm}$, and location of branching points at $60\,\mathrm{mm}$ and $105\,\mathrm{mm}$ (from the bottom of trunk to the bottom of the branches). The trees with eight branches at a 90 degree angle to the trunk and eight branches tilted upward at a 45 degree angle were included in the testing described

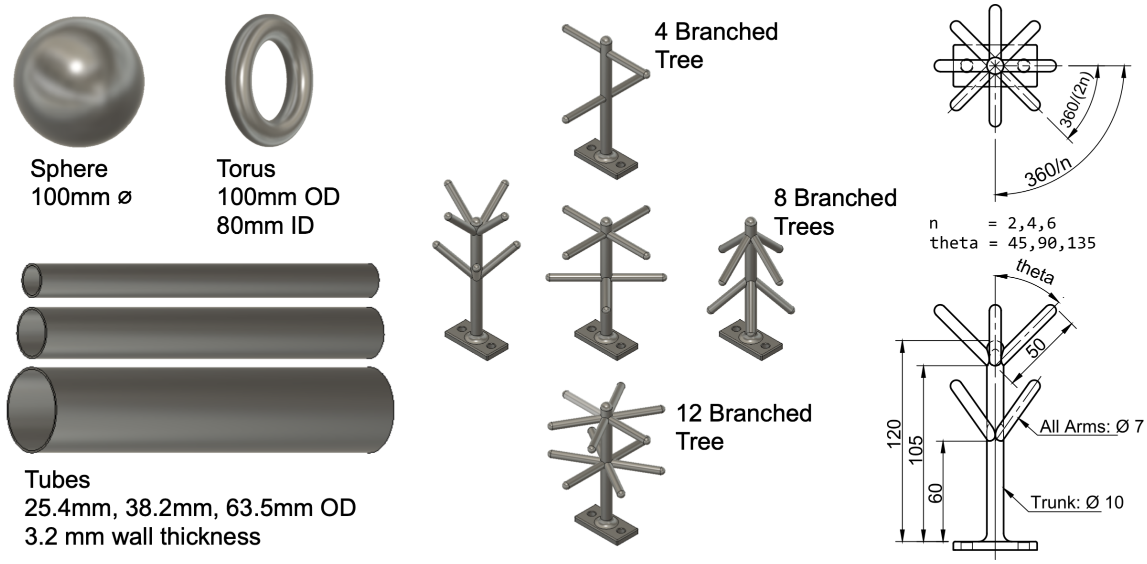

Supplementary Figure S1: Set of target objects used in testing. The dimensions and weights of the objects are listed in Table S1. Not shown are the Aluminum bars that were attached to the bottom of the tree structures for added weight for the robot arm grasp tests. These aluminum bars are visible in Figure 2 of the main text. Additionally, the dimensions (in mm and deg.) for one of the branched structures are shown in an engineering drawing. The number and angle of the branches changes for the other structures while all other dimensions are held constant.

Table S1: Physical properties of objects used in this study

Object	**Dimensions (mm)**	**Mass (g)**	**Material**
Sphere	100 diameter	10	Styrofoam
Tube	25 OD $\times$ 300 length	43	Polycarbonate
Tube	25 OD $\times$ 300 length	91	Polycarbonate
Tube	64 OD $\times$ 300 length	130	Polycarbonate
Torus	80 ID $\times$ 100 OD	69	PLA (3D printed)
Tree (8 branches, 45 deg)	80 width $\times$ 120 height	147	PLA + aluminum base
Tree (8 branches, 90 deg)	100 width $\times$ 100 height	148	PLA + aluminum base
Tree (8 branches, 135 deg)	80 width $\times$ 120 height	147	PLA + aluminum base
Tree (4 branches, 90 deg)	100 width $\times$ 120 height	144	PLA + aluminum base
Tree (12 branches, 90 deg)	100 width $\times$ 120 height	153	PLA + aluminum base

in the main text. The additional trees were used as target objects in similar tests described in the main text where a top drape approach was used and perfected object centering assumed. The results of these tests are discussed in the extended grasp strategy testing section below.

In addition to the set of objects used for laboratory and simulation grasp tests, the gripper was tested on target objects using a remotely operated arm and ROV in a deep-sea field test evaluation. This adds the complications of a different surrounding fluid, currents, unpredictable target objects, and limited testing vision and feedback. A twelve-filament array like the set used for the laboratory and simulated grasp success testing was successfully used to pick up a benthic sea star at a death of 800 m, which was then released after grasping. The field tests were performed with the help of the Schmidt Ocean Institute, the crew of the Falkor, the ROV pilots operating the vehicle SuBastien, and our collaborators from the URIL (Undersea Robotics & Imaging Laboratory) lab at the University of Rhode Island. Development of the entanglement gripper was originally motivated by the challenging grasping tasks the deep-sea, where the gentle grasps of deep sea life and precious artifacts cannot be done by human hands due to the hydrostatic pressure.

While the filament gripper was originally inspired by challenging deep-sea grasping tasks, the authors believe that entanglement grasping can also augment the abilities of robotic grasping with everyday objects on land which is the primary focus of this work. As discussed above, we have begun initial testing with a small subset of target objects. Rigorous testing with more complex objects, as well as discussion of how to classify the complexity of objects will be a subject of future study. The set of objects in figure S2 is intended to demonstrate the feasibility of using entanglement grasping for familiar household objects that might prove more challenging for the vast majority of robotic grippers, including an array of houseplants, irregularly shaped toys, and a flexible phone tripod. The grasping demonstrations below were not performed with a robot arm. To emulate a top drape approach while allowing the gripper to remain in a static position, the object was manually raised up into the array of unactuated filaments and the filaments were then pneumatically actuated around the object with an operating pressure of $25\,\mathrm{psi}$ ($172\,\mathrm{kPa}$).

Grasp Strategy Testing - Extended

We evaluated the performance of entanglement grasping using a task-based experimental and simulation approach. Analytical frameworks used to understand and plan grasps such as form and force closure, and contact curvature analysis become intractable with the large degree of randomness in contact interactions that entanglement relies upon. Experimental and simulation based evaluations allow for comparison with similar experimental studies used to evaluate traditional grippers. In defining an appropriate task, we use the common definition of a stable grasp: A grasp is statically-stable if the grasped object is in static equilibrium. Additionally, a common practical definition of grasp success during a manipulation task is used as a proxy for grasp stability since the actual force balance is intractable to

Supplementary Figure S2: Testing on some challenging objects.

measure in hardware: A grasp is successful if the target object is able to be moved from its initial position to a desired location without being dropped.

The first grasp tests performed, as described in the main text, evaluated three heuristic grasping approach strategies including the top drape, side-drape, and side-drape. A subset of the objects described above was presented in the main text and additional results showing the branched structure variants and performance with the three approach strategies are shown in figure S3. As with the tests presented in the main text, ideal conditions were assumed where the location of a target object is known and is centered with respect to the array of filaments in each of these additional tests. As with the previous tests, a top-drape approach was a slow lowering of the filaments onto the object and then actuation occurs, in a side-drape approach the filaments were lowered next to the object and then horizontally translated in the direction of the object to $50\,\mathrm{mm}$ past the center point of the object, and in a plop-on-top approach the filaments were first actuated above the object before being lowered to the intended grasp height and then released to fall around the object and actuate again for a grasp.

As can been seen in figure S3, the side-drape approach strategy gave the highest performance for all branched structures, with 100% grasp success rate for all but the eight branched tree with a $45\,\mathrm{deg}$ branch angle. The top-drape achieved higher performance for objects with more branches. The plop-on-top approach worked well for the tree with

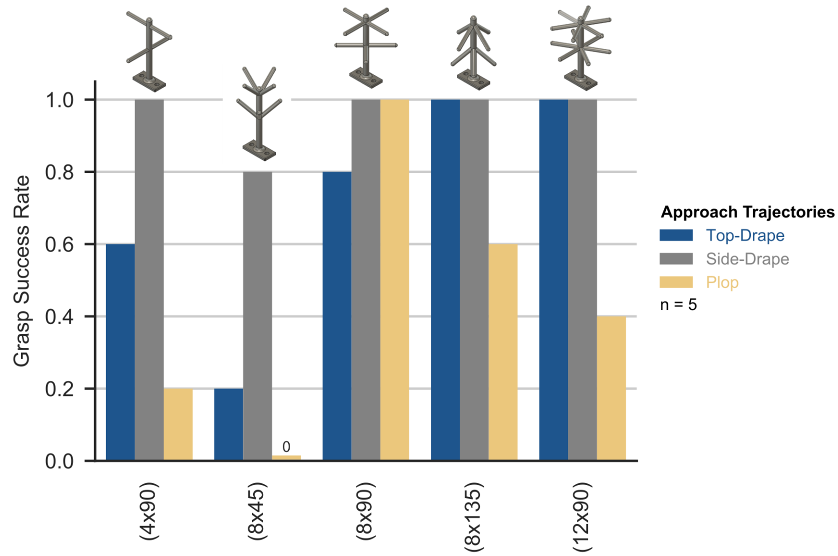

Supplementary Figure S3: Three heuristic grasping approach trajectories were evaluated on the set of branched objects using the same procedures as for the tests represented in Fig. 2b in the main text.

eight branches and branch angle of $90\,\mathrm{deg}$, but performance dropped off as both number of branches and angle of branches changed, up or down.

Another influential variable for future study is the height of the gripper at the point of actuation. Most of the robot arm mounted tests were performed with the tips of the filaments approximately aligned with the surface of the table. Shown in figure 3A, however, is another set of data taken from a physical centering test where the filaments were lowered -80mm below the point where they touched the table. This produced a significant increase in performance, where the grippers were able to retrieve the tree some portion of the time up to 50mm away from the center position (100% of the object radius). Some of the performance increase may be explained by the fact that, upon hitting the table, the filaments can splay outward, effectively extending their horizontal reach.

Pneumatic Actuation and Control

For repeatable and tuneable actuation of the filaments in the robot arm mounting grasp testing, the input pressure of our filament gripper was controlled by a custom pneumatic pressure control system based on the system used in the studies of Teeple et al. and Abondance et al.[3,4] The controller enables execution of arbitrary pressure trajectories in real time with an accuracy of $1.4\,\mathrm{kPa}$. The control system used in this work is shown in Figure S4. The working control range is between $-35\,\mathrm{kPa}$ and $350\,\mathrm{kPa}$, and preliminary testing shows this system has a response time of approximately $0.2\,\mathrm{s}$, enabling high-bandwidth operation. Finally, the system utilizes custom ROS drivers allowing high-level coordination between the gripper (pressure controller) and our robot arm. As this system is being actively developed at the time of writing, documentation about the hardware and software is available on GitHub.[5]

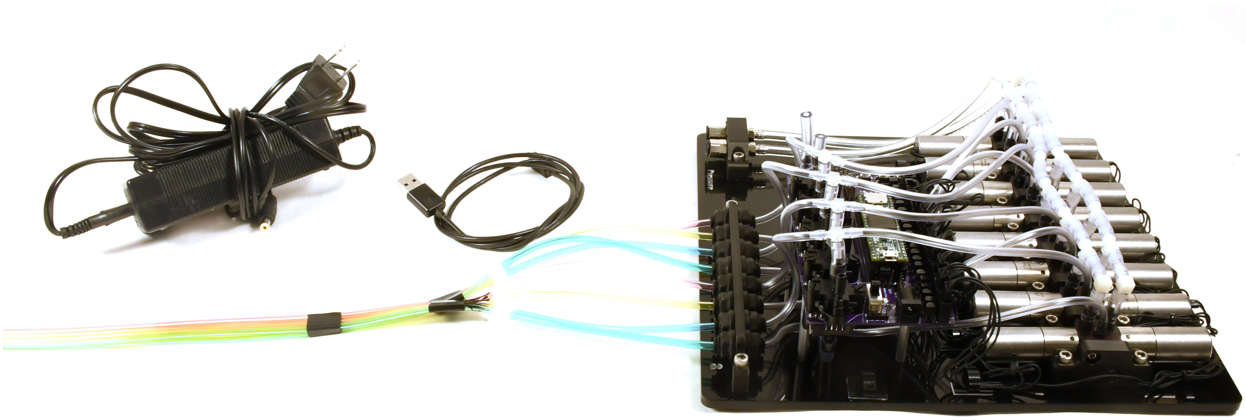

Supplementary Figure S4: The pressure control system used in this work is part of an ongoing, open-source project.[5] The system can control pneumatic pressure between $-35\,\mathrm{kPa}$ and $350\,\mathrm{kPa}$ with an accuracy of $1.4\,\mathrm{kPa}$ and a response time of $0.2\,\mathrm{s}$.

Object Pull Tests

As presented in the main text, grasping force tests were performed on an Instron material testing machine. Pictures of the test setup with a subset of the objects tested are shown in figure S5 along with plots of the raw force versus extension data. Only top drape approaches were performed because of the configuration limitations of the testing frame. The objects were also rigidly anchored, which was not true in the grasp success trials with the robot arm but the rigid anchoring provided a benchmark of the grip strength and a quantitative measurement to compare with simulation results. A summary of the average maximum gripping values observed from each trial as well as the maximum observed valued across all trials is summarized in Figure S6. The examples of the trial sets from which these values are derived, shown in figure S5, include the branched structure with eight limbs, the $63.5\,\mathrm{mm}$ diameter horizontal tube, the $25.4\,\mathrm{mm}$ diameter vertical tube, and the $63.5\,\mathrm{mm}$ diameter vertical tube.

As one might expect, the maximal gripping force achieve by the filament gripper was highly affected by the target object. Furthermore, the shape of the force versus extension curves shown in figure S5 reflects the nature of

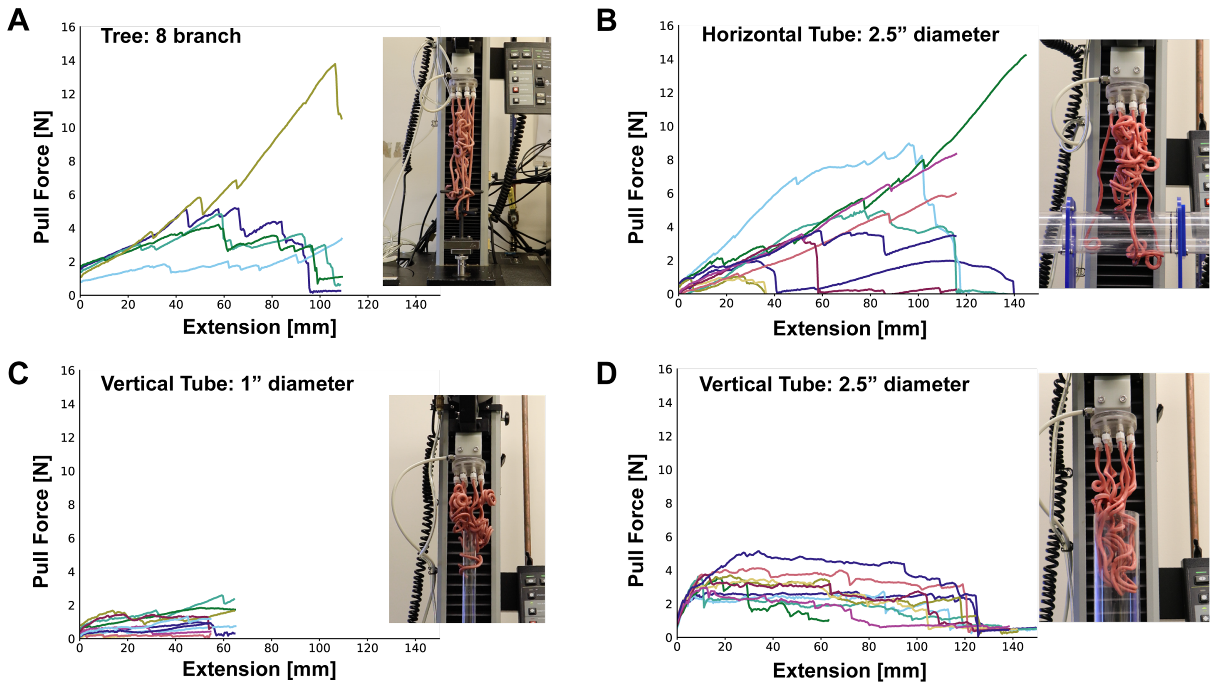

Supplementary Figure S5: Examples of the raw pull force data. The plots show how much force was exerted on an object as it was pulled out of the grasp of the twelve filament entanglement gripper. The corresponding test setup for each plot is shown in the pictures. Objects are rigidly mounted to bottom of test frame and the entanglement gripper is mounted to a load cell on a moving platform above the object. The objects shown are a) an eight branch tree, b) a horizontal $63.5\,\mathrm{mm}$ diameter tube, c) a vertical $25.4\,\mathrm{mm}$ diameter tube, and d)a vertical $63.5\,\mathrm{mm}$ diameter tube.

the engagement between the filaments and the object. For example, the filaments predominantly rely on friction to hold the vertical tubes. As the object is pulled from the gripper, the forces in figure S5C and figure S5D are relatively level and show the friction forces as the object slides through the grasp of the filaments. By contrast, the trials from the branched structure in figure S5A and horizontal tube in figure S5B appear to have a larger degree of variation that related to how many of the filaments wrapped around the tube or branches. There are also larger jumps in the data as individual filaments are pulled away and forced to release the object.

Using the shape of the data to discover information about an object may be an interesting direction for future study with entanglement grasping platforms. An example that could be investigated in greater depth is is a slight upward trend in the data form the $25.4\,\mathrm{mm}$ tube and a slight downward trend in the data of the $63.5\,\mathrm{mm}$ tube, which may possibly be explained by the way in which the filaments engage with the two objects. The testing setup associated with these two trial sets is shown in figure S5D and figure S5C. As shown in the pictures, the filaments were draped

	Average maximum value [N]	Maximum of maximum values [N]
4 Branch tree	3.92	6.03
8 Branch tree	6.86	16.18
12 Branch tree	9.14	12.66
8 Upward branch tree	2.306	4.68
8 Downward branch tree	5.99	13.42
1"⌀ Tube horizontal	6.85	27.64
2.5"⌀ Tube horizontal	8.65	34
1"⌀ Tube vertical	1.7	5.5
1.5"⌀ Tube vertical	6.98	8.64
2.5"⌀ Tube vertical	3.77	9.91
Sphere	0.76	2.06

Supplementary Figure S6: Maximum values observed in the grasping force tests. The left column is a the average of the maximum values observed for each set of trials and the right column is the maximum value observed over all trials. The trees with levels arms and the $38.1\,\mathrm{mm}$ vertical tube had five trials performed, all other objects had ten trials performed.

around the outside of the $25.4\,\mathrm{mm}$ tube but the $63.5\,\mathrm{mm}$ tube was large enough that they were lowered inside. As the filaments are pulled up from the object, their coils are extended, which would cause the coil diameter to contract and thereby cause a slight increase in forces as the filaments squeeze the outside of the smaller tube and decrease forces as the filaments pull away from the inner wall of the larger tube.

Grasp Toughness Metric

For the proposed grasp toughness metric, we used a trapezoidal approximation to numerically integrate the area under the averaged force-displacement curves of the grasp strength tests, such as the ones shown in Figure S5. The comparison values for the grasp toughness of soft grippers were similarly calculated from the data sets presented in prior soft gripper work, including the four-finger gripper with added tips around a $76\,\mathrm{mm}$ tube from Abondance et al.,[4] the two finger power grasp around a $51\,\mathrm{mm}$ tube from Teeple et al.,[3] and the two finger power grasp (with foam) around a $51\,\mathrm{mm}$ tube from Galloway et al.[6] It should be noted that these values are low estimates owing to the fact that the raw grip tests trials were truncated to the shortest release in order to more easily calculate an average value.

Contact Distribution

Randomly distributed contact points is a distinguishing feature of entanglement grasping with the filament gripper. This is difficult and time consuming to quantify in physical experiments but relatively easy to pull out of the simulation environment. For comparison between simulations and physical testing, we manually counted contact points on the four and eight branch tree objects. The filaments gripper was mounted onto a frame on top of a rotating platform and five pictures of the example grasps were taken at $45\,\mathrm{deg}$ increments. The camera remained stationary while the platform supporting the gripper and support structure were rotated. The objects were manually raised into the filaments to simulate a top drape approach with the fixed gripper mount. Two examples of the results are shown in Figure S7. The contacts were grouped by filament, as indicated by the letter and color. Individual contact point were visible in multiple views and thus have the same labels that appear in multiple images.

The contacts from the pictured eight branch object grasp in Figure S7 is also shown in Figure 3b, next to an example of simulated grasp of an eight branch structure in Figure 3c. In those examples shown, fourteen contact points are made by eight of the twelve gripper filaments. The range of contact points observed from successful grasp simulations was 11 to 32 discrete points of contact. This range of contacts was pulled from the results from the grasp test simulations represented in Figure 3C, where the density and branch length of the eight-branch tree and gripper filament spacing were varied. Not all contacts counted were necessarily load bearing, as can be inferred by the examples in Figure 3B, but this suggests that, for a given filament strength, there is a critical threshold of engagement or contacts that leads to a successful grasp and that number of contact points increases with target object weight. We have observed successful grasps with lower numbers of contacts from physical testing but this is dependent on the object weight and static friction, which is not represented in the simulation. The entanglement gripper performance and contact also changes with object shape, which we intend to characterize further in future work.

Simulation

We model each gripper filament using the Cosserat theory of elastic rods,[7,8] and solve the governing equations using the second order verlet numerical scheme used to model a variety of soft filaments.[9] The Cosserat theory allows us to capture the soft nature of the gripper filaments; in particular, it takes into account shear and stretch as well as the

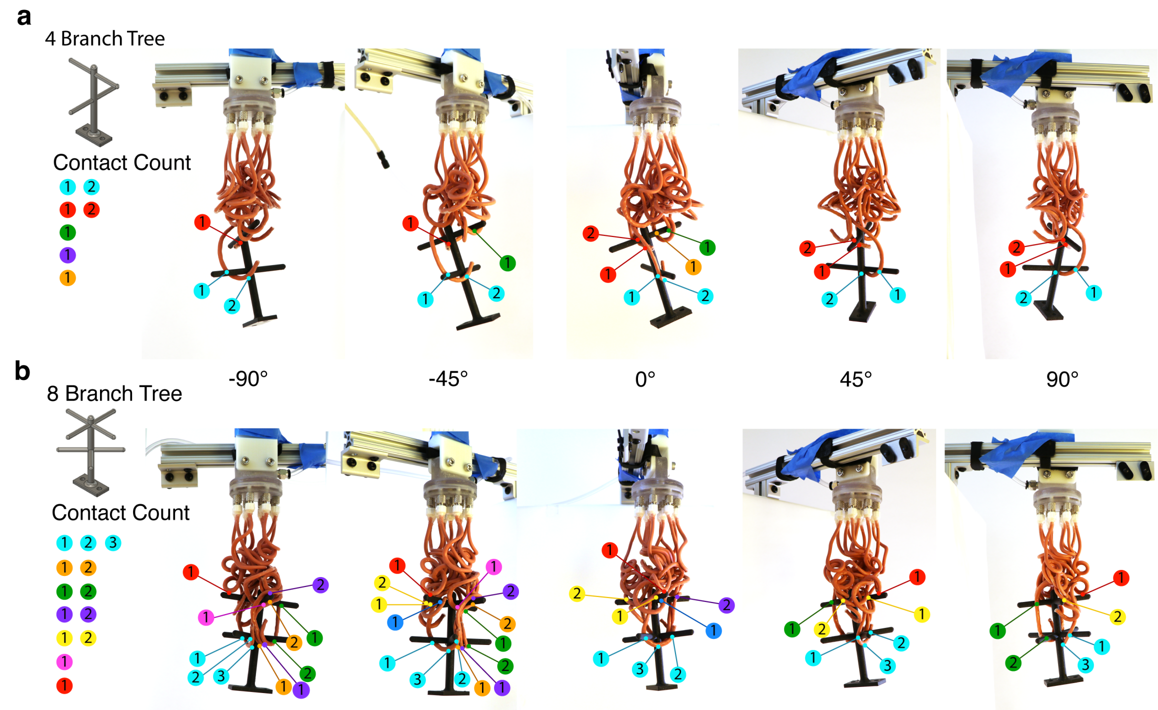

Supplementary Figure S7: Manual count of contact distribution of four branch tree from object set. The pictures are take at five different orientation, each 45 degrees apart. Individual contact points are counted and labeled. The contacts are group by the filament with which they are associated, indicated by the letter and color of the circle used to mark a contact point. The letter and number combination is unique to each contact and is repeated across pictures to show that the contact points are visible from multiple orientations. a) This is an example grasp on a four-branch tree and has seven contact points from five unique filaments on the twelve filament entanglement gripper.b) This is an example grasp on a eight-branch tree and has thirteen contact points from seven unique filaments on the twelve filament entanglement gripper.

more commonly modeled twisting and bending deformation modes. Below, we describe how we apply this simulation scheme to our gripper/target system.

We initialize twelve discretized gripper filaments, suspended vertically with their top ends clamped and all other centerline nodes free. The filaments are subject to gravity and mutual contact forces, including isotropic contact friction. The top ends are arranged in a planar array mimicking experimental setup. Below the plane of the bottom of the hanging gripper filaments, we initialize a branched target structure. Throughout the simulation, the target is subject to gravity. To keep the target from falling under gravity while the grippers attempt to grasp it, we use two environmental interactions: we simulate an infinite flat plane just below the base of the target's central rod (or "trunk") which interacts with the trunk via a hard contact interaction and contact friction. We also constrain the base of the trunk to remain in a vertical orientation until either (1) the filaments have fully actuated or (2) the base of the trunk is lifted more than $L_t/20$ above the plane, where L_t is the length of the trunk—whichever of those two conditions is met first. Hence, the trunk is kept vertical until the gripper has a chance to grasp the tree, but the tree is not constrained in a way that interferes with grasping.

At the start of a trial, the array of clamped gripper filaments' top ends is lowered until the filaments surround the target. The grippers are actuated by introducing intrinsic curvature everywhere along the length of the filaments at a constant rate, until a prescribed maximum intrinsic curvature is reached. The principal direction of curvature is constant over arclength with respect to the local filament cross-sectional frames, and is sampled randomly for each filament. The filaments relax elastically to their new state, adapting to their new intrinsic curvature while still being pulled downward by gravity. Note that we do not attempt to model the pressure-curvature relation exhibited by experimental filaments during actuation, but rather simulate actuation by directly prescribing nonzero filament intrinsic curvature.

In particular, the maximum intrinsic curvature varies as a function of arclength, with the maximum curvature value at each node drawn from a Gaussian distribution with mean $\mu_\kappa = 30\pi \frac{1}{\mathrm{m}}$ and standard deviation $\sigma_\kappa = \frac{1}{20}\mu_\kappa \frac{1}{\mathrm{m}}$. We also introduce a small random twist along the filament, causing small deviations in the principal direction of curvature and introducing a small amount of asymmetry needed for the helical buckling described below. Discretized twist values on each discretization edge are drawn from a Gaussian distribution with mean $0\frac{1}{\mathrm{m}}$ and standard deviation $\pi\frac{1}{\mathrm{m}}$. The mean principal direction of curvature (i.e. the direction of curvature with 0 twist insertion) is chosen randomly, as described above. As a result of non-deterministic curvatures, successive simulations with the same system parameters can produce different results. For systems in which the resulting grasp is tenuous, repeated simulations may produce qualitatively, in addition to quantitatively, different results, revealing the precarious nature of the grasp for those system parameters.

As the filaments relax to their new curved state, they initially curl in a nearly planar fashion. As they surpass a critical bending threshold, they buckle under their own weight into helical shapes. Under the correct conditions, filament coiling leads to entanglement between filaments as well as between the filaments and target, leading to a robust grasp, especially for soft targets and those with complex geometries.

To test grasp success, we lift the gripper upward by displacing the clamped filament ends, keeping the filaments actuated, and observe whether the gripper successfully displaces the target upward and holds it unsupported for a set length of time. We then return the filaments' curvature to zero, releasing the target. Note that if the target and filaments become sufficiently entangled, the target may not fall freely out of the gripper grasp after filament curvature returns to zero.

To simulate branched target structures, we model the trunk and each branch as an elastic filament and fully couple forces and torques at each branch joint. In particular, we initialize the structure's trunk and branches such that, at each joint, the rods being joined at that joint have exactly one node at the joint location. During simulation, the regions of each rod not located at joint locations are simulated as normal elastic rods. To update the positions of rod nodes and edges at joint locations, we first sum the masses, inertia matrices, forces and torques of all nodes and edges at the given joint. Using these summed quantities, we compute an updated position and velocity for the entire joint. We assign this updated joint position and velocity to each node and edge located at that joint. Hence, the nodes from different rods initialized at a given joint location are always updated identically, keeping the joint intact without the use of boundary conditions.

In Tables S2 and S3, we present the simulation parameters used to generate Fig. 3 and the supplementary video showing example simulations. Note that all parameters were chosen to match experimental measurements. The filaments' cross-section inner radius in the pressurized state is computed to keep the total cross-sectional area constant during actuation, as observed in experiment. Also note that $A_{\text{rest}} = \pi\left(R^{\text{o}}_{\text{rel}} r^{\text{o}}_{\text{rel}} - \left(r^{\text{i}}_{\text{rel}}\right)^2\right)$ denotes cross-sectional area during the relaxed state.

Using the method described in[9] and,[10] we use translational and angular linear external damping, and no internal damping. In particular, we apply a linear translational damping force $\mathbf{F}_{\text{damp}} = -\left(\gamma_t L_{\text{f}}/n_{\text{f}}\right)\mathbf{v}$, where $\mathbf{v}$ is local filament velocity, L_{f} is filament length, n_{f} is filament discretization elements, and γ_t is the translational damping coefficient. Independent of $\mathbf{F}_{\text{damp}}$, we also apply a linear angular damping torque $\mathbf{M}_{\text{damp}} = -\left(\gamma_a L/n\right)\boldsymbol{\omega}$, where $\boldsymbol{\omega}$ is the local filament angular velocity and γ_a is the angular damping coefficient. For reference, following the derivation in the SI of,[10] we compute characteristic damping scales $\gamma_t^{\text{char}} = r^2\sqrt{E\pi^3\lambda/(4L^4)}$ and $\gamma_a^{\text{char}} = L^2\gamma_t^{\text{char}}$, where λ is mass per unit length and r is radius. For gripper filaments, we use $r = r^o_{\text{rel}}$ and obtain $\gamma_t^{\text{char}} = 1.726 \cdot 10^{-2}\ \frac{\text{kg}}{\text{m}\cdot\text{s}}$ and $\gamma_a^{\text{char}} = 1.153 \cdot 10^{-3}\ \frac{\text{kg}\cdot\text{m}}{\text{s}}$. For target trees, we use $L = L_{\text{t}} = 1.2 \cdot 10^{-2}$ m, $\lambda = \rho_{\text{tree}}\pi\bar{r}^2_{\text{tree}} = 1.309 \cdot 10^{-1}$ kg/m, $r = \bar{r}_{\text{tree}}$, where $\bar{r}_{\text{tree}}$ is mean tree radius (since tree radius varies over phase space), and ρ_{tree} is tree mass density, to obtain $\gamma_t^{\text{char}} = 9.579 \cdot 10^4\ \frac{\text{kg}}{\text{m}\cdot\text{s}}$ and $\gamma_a^{\text{char}} = 13.793\ \frac{\text{kg}\cdot\text{m}}{\text{s}}$.

Table S2: Simulation settings for gripper filaments

length L_{f}	$2.585 \cdot 10^{-1}$ m
inner radius (relaxed) $r^{\text{i}}_{\text{rel}}$	$7.038 \cdot 10^{-4}$ m
outer radius (relaxed, major axis) $R^{\text{o}}_{\text{rel}}$	$2.15 \cdot 10^{-3}$ m
outer radius (relaxed, minor axis) $r^{\text{o}}_{\text{rel}}$	$2.02 \cdot 10^{-3}$ m
inner radius (pressurized) $r^{\text{i}}_{\text{pres}}$	$\sqrt{r^{\text{o}}_{\text{pres}} R^{o}_{\text{pres}} - (A_{\text{rest}}/\pi)}$
outer radius (pressurized, major axis) $R^{\text{o}}_{\text{pres}}$	$3.075 \cdot 10^{-3}$ m
outer radius (pressurized, minor axis) $r^{\text{o}}_{\text{pres}}$	$2.375 \cdot 10^{-3}$ m
Young's modulus E	$6.246 \cdot 10^5$ Pa
shear modulus G	$E/3$
shear/stretch matrix **B**	diag$(4GA/3, 4GA/3, EA)$ N
bend/twist matrix **S**	diag(EI_1, EI_2, GI_3) Nm^2
discretization elements n_{f}	130
translational damping γ_t	$2.00 \cdot 10^{-2}\ \frac{\text{kg}}{\text{m}\cdot\text{s}} = 1.159\gamma_t^{\text{char}}$
angular damping γ_a	$1.00 \cdot 10^{-2}\ \frac{\text{kg}\cdot\text{m}}{\text{s}} = 8.673\gamma_a^{\text{char}}$
mass per unit length λ	$1.65 \cdot 10^{-2}$ kg/m
gravitational strength g	9.8 N/kg
time discretization δt	$\left(0.005\frac{\text{s}}{\text{m}}\right) L_{\text{f}}/n_{\text{f}}$ seconds

References

[1] K. P. Becker, Y. Chen, and R. J. Wood, "Soft actuator arrays: Mechanically programmable dip molding of high aspect ratio soft actuator arrays (adv. funct. mater. 12/2020)," *Advanced Functional Materials*, vol. 30, no. 12, p. 2070075, 2020.

[2] B. Calli, A. Walsman, A. Singh, S. Srinivasa, P. Abbeel, and A. M. Dollar, "Benchmarking in manipulation research: Using the yale-cmu-berkeley object and model set," *IEEE Robotics & Automation Magazine*, vol. 22, no. 3, pp. 36–52, 2015.

[3] C. B. Teeple, T. N. Koutros, M. A. Graule, and R. J. Wood, "Multi-segment soft robotic fingers enable robust precision grasping," *The International Journal of Robotics Research*, 2020.

Table S3: Simulation settings for target tree

trunk length L_{t}	$1.2 \cdot 10^{-1}$ m
mean branch length $\bar{L}_{\mathrm{b}}$ (varies in phase space)	$5 \cdot 10^{-2}$ m
mean trunk radius $\bar{r}_{\mathrm{tree}}$	$5 \cdot 10^{-3}$ m
mean branch radius $\bar{r}_{\mathrm{branch}}$	$3.5 \cdot 10^{-3}$ m
Young's modulus E_{tree}	$3.0 \cdot 10^{7}$ Pa
shear modulus G	$E/3$
shear/stretch matrix **B**	diag$(4GA/3, 4GA/3, EA)$ N
bend/twist matrix **S**	diag(EI_1, EI_2, GI_3) Nm^2
trunk discretization elements n_{t}	15
branch discretization elements n_{b}	$15L_b/\bar{L}_b$
translational damping γ_t	$2.00 \cdot 10^{-3}\ \frac{\mathrm{kg}}{\mathrm{m \cdot s}} = 2.09 \cdot 10^{-8}\gamma_t^{\mathrm{char}}$
angular damping γ_a	$2.00 \cdot 10^{-3}\ \frac{\mathrm{kg \cdot m}}{\mathrm{s}} = 1.45 \cdot 10^{-4}\gamma_a^{\mathrm{char}}$
mass density ρ_{tree} (varies in phase space)	16.67kg/m^3
gravitational strength g	9.8 N/kg
time discretization δt	$\left(0.001\frac{\mathrm{s}}{\mathrm{m}}\right) L_{\mathrm{f}}/n_{\mathrm{f}}$ seconds

[4] S. Abondance, C. B. Teeple, and R. J. Wood, "A dexterous soft robotic hand for delicate in-hand manipulation," *IEEE Robotics and Automation Letters*, vol. 5, no. 4, pp. 5502–5509, 2020.

[5] C. B. Teeple, "Ctrl-p: Smooth pressure control for soft robots," *Computer Software*, April. 2020.

[6] K. C. Galloway, K. P. Becker, B. Phillips, J. Kirby, S. Licht, D. Tchernov, R. J. Wood, and D. F. Gruber, "Soft Robotic Grippers for Biological Sampling on Deep Reefs," *Soft Robotics*, vol. 3, no. 1, p. soro.2015.0019, 2016.

[7] E. Cosserat and F. Cosserat, *Théorie des corps déformables*. A. Hermann et fils,, 1909.

[8] O. M. O'Reilly, *Modeling Nonlinear Problems in the Mechanics of Strings and Rods: The Role of the Balance Laws*. Interaction of Mechanics and Mathematics, Cham: Springer International Publishing, 2017.

[9] M. Gazzola, L. H. Dudte, A. G. Mccormick, and L. Mahadevan, "Forward and inverse problems in the mechanics of soft filaments.," *Roy. Soc. Open Sci.*, vol. 5, p. 171628, 2018.

[10] N. Charles, M. Gazzola, and L. Mahadevan, "Topology, geometry, and mechanics of strongly stretched and twisted filaments: Solenoids, plectonemes, and artificial muscle fibers," *Physical review letters*, vol. 123, no. 20, p. 208003, 2019.